Initial Orbit Determination from Ephemeris Models: Accurate Reconstruction of Maneuvering Cislunar Orbits Using Nonlinear Programming

Casey R. Heidrich and Marcus J. Holzinger
University of Colorado Boulder, Boulder, CO USA

ABSTRACT

Efficient numerical methods for initial orbit determination (IOD) are essential for safe operations in cislunar space. IOD approaches leveraging sparse grid collocation and nonlinear programming have shown promise for solving challenging cislunar orbit determination problems. However, these have relied on simplifying assumptions, namely two-body or circular restricted three-body dynamics. These assumptions reduce the applicability of prior methods to realistic spacecraft orbits in the Earth-Moon system. This work considers a high-fidelity IOD framework that operates directly on ephemeris models derived from the NASA SPICE toolkit. In addition, a novel extension to collocation-based IOD methods is developed by introducing control estimation techniques with velocity impulses applied along optimized maneuver directions. These approaches enable accurate tracking of active spacecraft without prior knowledge of maneuvers. Applications relevant to cislunar SSA highlight the value of this framework for tracking spacecraft in multi-body orbital regimes. The reconstructed state and control histories are compared to independent sources of data published from historical missions to verify the accuracy of the method.

1. INTRODUCTION

Initial orbit determination (IOD) remains a continuing challenge in cislunar space situational awareness (SSA). A reliable SSA architecture must accurately compute orbits of observed spacecraft from optical or radio frequency measurements to predict future motion. Traditional IOD methods, such as Gauss or double-r methods [1], were developed under two-body assumptions. These assumptions break down for the highly chaotic and complex orbits of cislunar space. This complexity has motivated growing efforts in the literature [2] to develop novel and effective methods for cislunar IOD. Recent work in cislunar orbit determination has leveraged machine learning aided strategies [3, 4, 5, 6], probabilistic and statistical methods [7, 8, 9], and iterative numerical methods [10, 11]. These works have generally targeted improvements to the accuracy and reliability of reconstructed orbits in cislunar space. A common difficulty in cislunar IOD involves prediction of motion across large observing gaps. Non-Keplerian dynamics introduce chaotic behavior, which becomes difficult to predict in optimization-based algorithms. Additionally, unmodeled maneuvers can lead to divergence from assumed dynamics models. To address these challenges, continuing work must focus on advancing IOD methods for applications with dynamical inconsistency and inherent chaos.

In this work, we focus on a class of IOD algorithms built upon sparse grid collocation methods [12, 13]. Unlike explicit integration methods that "march" a solution forward or backward in time, the collocation IOD approach implicitly enforces system dynamics through transcription constraints. The resulting solution can be rapidly computed using interior-point solvers. One of the primary benefits of the approach is to eliminate the need for a close initial guess. For example, solver convergence is sufficient for a wide range of orbits beginning with initialization at one of the Earth-Moon Lagrange points. Recent applications to agile spacecraft trajectories [13] have demonstrated reliability for IOD with impulsive or continuous low-thrust maneuvers. Control reconstruction is a highly valuable tool for understanding spacecraft thrust capability and predicting future motion.

Although collocation-based IOD methods have shown promise for solving complex IOD problems, prior applications have largely been limited to simplified dynamics models such as the circular restricted three-body problem (CR3BP). CR3BP dynamics are widely used and validated in cislunar mission analysis, but they can be inaccurate for realistic observing applications. For example, the small eccentricity of the Earth-Moon orbit gradually changes the relative

Approved for public release; distribution is unlimited. Public Affairs release approval AFRL-2025-4052. The views expressed are those of the authors and do not reflect the official guidance or position of the United States Government, the Department of Defense or of the United States Air Force.

distance between the two bodies over the course of one sidereal period, violating circular assumptions. External perturbations including the sun's gravity and solar radiation pressure will also influence spacecraft motion. Generalizations such as the elliptic three-body problem [14] and bi-circular four-body problem [15] can offer some improvements to model accuracy, at the expense of computational complexity and geometric insight of the CR3BP. However, NASA's NAIF SPICE toolbox [16] is widely considered the gold standard in modeling planetary ephemerides for space mission design and observation. Given the need for operational reliability of IOD algorithms, we are motivated to develop an approach taking advantage of both: (a) high-fidelity ephemeris models offered by SPICE for realistic observer positioning and physics modeling, and (b) computational reliability and efficiency of collocation-based IOD algorithms to perform spacecraft tracking and maneuver reconstruction.

This work seeks to develop accurate and efficient IOD methods for cislunar space directly leveraging planetary ephemeris models. First, we discuss relevant reference frames and SPICE configuration data. We then develop rotating frame dynamics without relying on planar or circular orbit assumptions from the CR3BP. The approach is general, allowing for modeling of arbitrary external perturbing forces depending on the domain of application. Collocation-based methods are then applied to the ephemeris-derived rotating frame dynamics to model the time evolution of cislunar trajectories. The resulting solution can then be transformed back into an inertial frame for comparison. Initial results show accurate reconstruction from simulated measurements for realistic spacecraft orbits, using archival data from the NASA JPL Horizons ephemeris system [17]. Results are validated against historical data for missions with documented maneuvers. Collocation-based IOD utilizing ephemerides provides significant potential for improving cislunar SSA capabilities by leveraging high-fidelity models for orbit determination in realistic spacecraft tracking applications.

2. EARTH-MOON ROTATING FRAME DYNAMICS

Application of collocation-based IOD methods to realistic observing applications requires developing equations of motion that accurately account for the positions of gravitational bodies over time. From an optimization perspective, it is beneficial to describe this motion in a rotating frame relative to the Earth-Moon system. Generalizations of the CR3BP allow for greater model accuracy by relaxing assumptions for circular orbits or adding fourth-body effects. Such models include the elliptic restricted three-body problem (ER3BP) and bi-circular restricted four-body problem (BCR4BP), among others. Although the analytic form of these equations may provide some theoretical insight to the equations of motion, these models rely on assumptions of motion for primary and secondary bodies that may not accurately reflect long-term evolution of solar system dynamics. The most widely accepted models of spacecraft dynamics for realistic spaceflight applications leverage high-fidelity ephemeris models for planetary motion. Equations of motion are commonly represented in an inertial frame such as J2000, although prior works develop the pulsating-rotating frame to account for relative motion in a frame fixed to the Earth-Moon system [18, 19]. However, it requires a non-trivial mapping of expressions to physical quantities, such as pulsating distance, rotation, and translation, and their associated rates of change.

In this section, we derive the Earth-Moon (EM) rotating frame definition from a dynamical systems perspective using a relative motion description. A depiction of this frame is illustrated in Fig. 1. The approach offers two benefits. First, application of Newton's second law in the rotating frame makes including new forcing terms straightforward. Second, terms are easily mapped to outputs from SPICE with minimal abstraction, allowing for easier implementation.

To begin, let us first define the inertial J2000 frame as $\mathbb{N}:\{\hat{\boldsymbol{n}}_1,\hat{\boldsymbol{n}}_2,\hat{\boldsymbol{n}}_3\}$. Similarly, the EM frame $\mathbb{S}:\{\hat{\boldsymbol{i}},\hat{\boldsymbol{j}},\hat{\boldsymbol{k}}\}$ is defined from the basis vectors

$$^{\mathbb{N}}\hat{\boldsymbol{i}}=\frac{^{\mathbb{N}}\boldsymbol{r}_{EM}}{\|\boldsymbol{r}_{EM}\|},\quad ^{\mathbb{N}}\hat{\boldsymbol{j}}=^{\mathbb{N}}\hat{\boldsymbol{k}}\times^{\mathbb{N}}\hat{\boldsymbol{i}},\quad \hat{\boldsymbol{k}}=\frac{^{\mathbb{N}}\boldsymbol{h}_{EM}}{\|\boldsymbol{h}_{EM}\|}. \tag{1}$$

For all frame definitions, we will assume they are centered at the Earth-Moon barycenter unless otherwise noted. The quantity $\boldsymbol{r}_{EM}$ denotes the relative position between the Earth and Moon, expressed in N-frame coordinates. Similarly, $\boldsymbol{h}_{EM}$ represents the instantaneous specific angular momentum vector of the primary motion, computed as $\boldsymbol{h}_{EM}=\boldsymbol{r}_{EM}\times\boldsymbol{v}_{EM}$. The rotation from the $\mathbb{N}$ to $\mathbb{S}$ frame can be computed from the direction cosine matrix (DCM)

$$[C]=\left[^{\mathbb{N}}\hat{\boldsymbol{i}},\quad ^{\mathbb{N}}\hat{\boldsymbol{j}},\quad ^{\mathbb{N}}\hat{\boldsymbol{k}}\right]^{\mathrm{T}}. \tag{2}$$

We can now apply relative motion equations to the rotating frame. First, define $\boldsymbol{r}$ and $\boldsymbol{v}$ as the relative position and

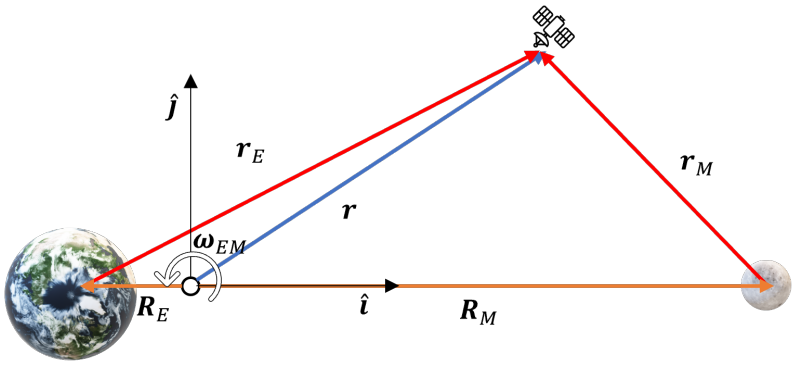

Fig. 1: Schematic of two-vector EM frame derived from SPICE ephemerides.

velocity vectors, respectively, as seen by the EM frame. Denote the Earth-Moon barycenter O as the origin of the frame. The total velocity of the spacecraft as seen by the inertial frame is

$$\boldsymbol{v}_{tot} = \boldsymbol{v}_O + \boldsymbol{v} + \boldsymbol{\omega}_{EM} \times \boldsymbol{r}, \tag{3}$$

where $\boldsymbol{v}_O$ is the inertial velocity of the frame origin (assumed zero), and $\boldsymbol{\omega}_{EM}$ is the angular velocity of the $\mathbb{S}$ frame as seen by the $\mathbb{N}$ frame. Taking a time derivative of Eq. (3) gives a well-known expression for acceleration in a moving frame of reference [20]

$$\boldsymbol{a}_{tot} = \boldsymbol{a}_O + \boldsymbol{a} + 2\boldsymbol{\omega}_{EM} \times \boldsymbol{v} + \boldsymbol{\alpha}_{EM} \times \boldsymbol{r} + \boldsymbol{\omega}_{EM} \times (\boldsymbol{\omega}_{EM} \times \boldsymbol{r}), \tag{4}$$

where $\boldsymbol{a}_O$ is the inertial acceleration of the frame origin (assumed zero), and $\boldsymbol{\alpha}_{EM}$ is the angular acceleration of the $\mathbb{S}$ frame as seen by the $\mathbb{N}$ frame. Note that Eqs (3) and (4) are written without a frame specification; henceforward, we will assume vector quantities without a prescript are expressed in rotating frame coordinates, unless otherwise stated.

Next, consider the forces acting on the spacecraft. We assume the Earth and Moon gravity influences follow Newton's law of gravity (i.e., classical two-body point mass models)

$$\boldsymbol{F}_E = -\frac{mGM_E}{\|\boldsymbol{r}_E\|^3}\boldsymbol{r}_E, \quad \boldsymbol{F}_M = -\frac{mGM_M}{\|\boldsymbol{r}_M\|^3}\boldsymbol{r}_M. \tag{5}$$

GM_E and GM_M are the gravity mass products and $\boldsymbol{r}_E$ and $\boldsymbol{r}_M$ are the position vectors of the spacecraft with respect to the Earth and Moon, respectively. These vectors are computed as $\boldsymbol{r}_E = \boldsymbol{r} - \boldsymbol{R}_E$ and $\boldsymbol{r}_M = \boldsymbol{r} - \boldsymbol{R}_M$, where $\boldsymbol{R}_E$ and $\boldsymbol{R}_M$ are the absolute position vectors of each primary with respect to the coordinate frame origin O. We also consider tidal effects of the Sun's gravity on the rotating frame dynamics. Because the inertial origin of the frame is not assumed coincident with the Earth-Moon-Sun system barycenter, we define the effects of the Sun's gravity as its relative influence on the system barycenter and spacecraft:

$$\boldsymbol{F}_{S,rel} = -\frac{mGM_S}{\|\boldsymbol{R}_S\|^3}\boldsymbol{R}_S - \frac{mGM_S}{\|\boldsymbol{r}_S\|^3}\boldsymbol{r}_S. \tag{6}$$

In this expression, $\boldsymbol{r}_S$ is the position of the spacecraft relative to the Sun, and $\boldsymbol{R}_S$ is the absolute position vector of the Sun relative to the coordinate frame origin O.

Applying Newton's second law in the rotating frame and solving Eq. (4) for the relative acceleration $\boldsymbol{a}$, we complete the equations of motion for the spacecraft dynamics as

$$\begin{bmatrix}\dot{\boldsymbol{r}}\\ \dot{\boldsymbol{v}}\end{bmatrix} = \boldsymbol{f}(\boldsymbol{x}(t),t) = \begin{bmatrix}\boldsymbol{v}\\ -2\boldsymbol{\omega}_{EM} \times \boldsymbol{v} - \boldsymbol{\alpha}_{EM} \times \boldsymbol{r} - \boldsymbol{\omega}_{EM} \times (\boldsymbol{\omega}_{EM} \times \boldsymbol{r}) + \frac{1}{m}\left(\boldsymbol{F}_E + \boldsymbol{F}_M + \boldsymbol{F}_{S,rel}\right)\end{bmatrix}. \tag{7}$$

The state vector $\boldsymbol{x} = [\boldsymbol{r},\ \boldsymbol{v}]^{\mathrm{T}}$ comprises the position and velocity vectors in the rotating frame. Equation (7) provides a relative motion description of the EM frame, with no generalizations or assumptions on the description of motion (i.e., circular or elliptical orbits, co-planar orbits). The forces modeled in the system include gravitational influences of the Earth and Moon, as well as the tidal effect of the Sun's gravity. It is straightforward to add additional forcing

Table 1: Parameters used in SPICE functions for frame of reference, aberration correction, and observing body.

Parameter	Value
`ref`	`"EM"`
`abcorr`	`"NONE"`
`obs`	`"EARTH-MOON BARYCENTER"`

terms as needed. For our SSA-inspired application, these forcing terms adequately describe the four-body dynamics of spacecraft motion in the EM frame. In the next section, we outline procedures to generate required terms in these expressions from high-fidelity ephemeris models.

3. INCORPORATING HIGH-FIDELITY EPHEMERIDES

In order to evaluate the EM rotating frame dynamics, we require several physical quantities derived from the solar system state at a given epoch. These quantities are computed using the SPICE toolkit. First, the EM frame is defined in SPICE as a two-vector frame. The primary vector is defined by the Moon position relative to the Earth-Moon barycenter. The secondary vector is defined by the Moon J2000 velocity relative to the Earth-Moon barycenter. Table 1 shows relevant parameters used in SPICE computation, and Table 2 outlines relevant function calls used to compute quantities of interest.

Table 2: Computation of ephemeris-based quantities using NASA SPICE toolkit.

Parameter(s)	Description	SPICE Computation
GM_E, GM_M	Planetary physical constants.	`bodvrd(bodynm, "GM", 3)`
$[X]$	State transformation matrix from $\mathbb{N}$ to $\mathbb{S}$ frame.	`sxform("J2000", ref, et)`
$[C]$, ${}^{\mathbb{N}}\boldsymbol{\omega}_{EM}$	Rotation matrix and angular velocity of $\mathbb{S}$ frame expressed in $\mathbb{N}$ frame coordinates.	`xf2rav(xform)`
$\boldsymbol{R}_E$, $\boldsymbol{R}_M$	Position of Earth and Moon relative to EM coordinate frame origin.	`spkezr(targ, et, ref, abcorr, obs)`

The state transformation matrix $[X]$ provided by the `sxform` function in SPICE has the form

$$[X] = \begin{bmatrix} [C] & [0_{3\times 3}] \\ [\tilde{\boldsymbol{\omega}}][C] & [C] \end{bmatrix}, \tag{8}$$

where $[\tilde{\boldsymbol{\omega}}]$ is the skew-symmetric cross product matrix defined as

$$[\tilde{\boldsymbol{\omega}}] = \begin{bmatrix} 0 & -\omega_3 & \omega_2 \\ \omega_3 & 0 & -\omega_1 \\ -\omega_2 & \omega_1 & 0 \end{bmatrix}. \tag{9}$$

The angular velocity vector expressed in $\mathbb{N}$ frame coordinates can be easily computed using the `xf2rav` function in SPICE. However, we also require the angular velocity vector of the EM frame expressed in $\mathbb{S}$ frame coordinates. This vector can be computed by the transformation

$$\boldsymbol{\omega}_{EM} = [C] \cdot {}^{\mathbb{N}}\boldsymbol{\omega}_{EM}, \tag{10}$$

which represents a rotation of the angular velocity vector from inertial to rotating frame coordinates.

Next, we require the angular acceleration of the EM frame. Taking a time derivative of Eq. (10), we find

$$\boldsymbol{\alpha}_{EM} = \frac{\mathrm{d}}{\mathrm{d}t}\left([C]\right) \cdot {}^{\mathbb{N}}\boldsymbol{\omega}_{EM} + [C] \cdot {}^{\mathbb{N}}\boldsymbol{\alpha}_{EM}. \tag{11}$$

From this expression, we can find the rotation matrix time derivative $\mathrm{d}([C])/\mathrm{d}t$ from the bottom left matrix entry in Eq. (8). The angular acceleration vector ${}^{\mathbb{N}}\boldsymbol{\alpha}_{EM}$ is not as straightforward. Angular acceleration of a two-vector frame is not provided directly by SPICE (this was confirmed through correspondence with NAIF). The first and simplest approach is to compute a finite difference approximation of the angular acceleration vector at each required epoch. For a small step size h, a forward difference approximation is

$$ {}^{\mathbb{N}}\boldsymbol{\alpha}_{EM} \approx \frac{{}^{\mathbb{N}}\boldsymbol{\omega}_{EM}(t+h) - {}^{\mathbb{N}}\boldsymbol{\omega}_{EM}(t)}{h}. \tag{12} $$

However, the finite difference approximation is often noisy and inaccurate, which can introduce numerical errors in solution. A second and more reliable approach is to construct a B-spline approximation. As part of the collocation-based method in the following section, we discretize the time domain into nodes t_k for $k = 1,\ldots,N$. The angular velocity vectors from SPICE are sampled at node times ${}^{\mathbb{N}}\boldsymbol{\omega}_{EM,k}$. A cubic B-spline basis is then constructed as

$$ {}^{\mathbb{N}}\boldsymbol{\omega}_{EM}(t) \approx \sum_{i=1}^{M} \boldsymbol{\gamma}_i D_i(t), \tag{13} $$

where $D_i(t)$ are C^1 basis functions with $M = 2N$, and $\boldsymbol{\gamma}_i$ are interpolation coefficients. A smooth approximation of the angular acceleration as a function of time can be computed as

$$ {}^{\mathbb{N}}\boldsymbol{\alpha}_{EM}(t) \approx \sum_{i=1}^{M} \boldsymbol{\gamma}_i \frac{\mathrm{d}D_i(t)}{\mathrm{d}t}. \tag{14} $$

It is then straightforward to compute the angular acceleration sampled at nodes times t_k as ${}^{\mathbb{N}}\boldsymbol{\alpha}_{EM,k} = {}^{\mathbb{N}}\boldsymbol{\alpha}_{EM}(t_k)$. This formulation ensures both angular velocity and angular acceleration are smoothly approximated by cubic and quadratic splines, respectively. For further information regarding interpolation methods as they relate to dynamic transcription problems, the reader is referred to Betts [21, Ch. 4]

4. COLLOCATION-BASED INITIAL ORBIT DETERMINATION

Solution of initial orbits for spacecraft in the cislunar regime can present challenges due to the chaotic, unpredictable behavior of multi-body gravity dynamics. Numerical IOD methods based on explicit forward integration tend to break down in these systems, particularly over long timescales. To overcome these challenges, a recent study explored direct transcription and collocation methods for solving sensitive IOD problems [12]. The approach approximates system trajectories using collocation constraints. A discrete transformation of the IOD problem can be posed as a large-scale sparse nonlinear programming (NLP) problem. A primary benefit of this approach is to remove the need for a close initial guess, due to the large region of convergence enabled by NLP solvers.

In this section, we briefly review collocation-based IOD methods in the context of SSA. Then, we propose a modified maneuver estimation technique to account for impulsive maneuvers acting along an unknown line of action. This modification allows us to model larger, more realistic burns for spacecraft performing significant trajectory corrections within the IOD solver.

4.1 Transcription Methods for Continuous Functions

First, consider the discretized time interval for N nodes:

$$ t_k = t_1 < t_2 < \cdots < t_N. \tag{15} $$

Corresponding to this discretization, the system states at each node time are appended as unknown NLP parameters. Integration of the differential system dynamics function (i.e., Eq. (7)) is replaced by so-called defect constraints, which enforce integration between nodes using numerical quadrature rules. For example, Hermite-Simpson collocation approximates the system dynamics with quadratic splines, resulting in the following transcription between nodes k and $k+1$.

$$ \boldsymbol{x}_{k+1} - \boldsymbol{x}_k - \frac{1}{6} h_k \left(\boldsymbol{f}_k + 4\boldsymbol{f}_{k+1/2} + \boldsymbol{f}_{k+1} \right) = \boldsymbol{0} \quad \text{for} \quad k = 1,\ldots,N-1, \tag{16} $$

where $h_k = t_{k+1} - t_k$ is the interval step size and $\boldsymbol{f}_k = \boldsymbol{f}(\boldsymbol{x}_k, t_k)$ is the system dynamics evaluated at time $t = t_k$. Equation (16) also requires an evaluation of the state at the midpoint time $t_{k+1/2} = (t_{k+1} + t_k)/2$. In *compressed* form, the midpoint states can be evaluated by a Hermite polynomial interpolant as

$$\boldsymbol{x}_{k+1/2} = \frac{1}{2}(\boldsymbol{x}_k + \boldsymbol{x}_{k+1}) + \frac{1}{8}(\boldsymbol{f}_k - \boldsymbol{f}_{k+1}). \tag{17}$$

The non-maneuvering IOD problem considers a least squares objective that minimizes the weighted measurement residuals at each observation. A general nonlinear measurement model is assumed of the form

$$\boldsymbol{y}_i = \boldsymbol{h}(\boldsymbol{x}_i, t_i), \tag{18}$$

which for a sequence of observations $\{\boldsymbol{y}_1, \boldsymbol{y}_2, \ldots, \boldsymbol{y}_p\}$ the optimization objective is

$$\Phi(\boldsymbol{x}, \ldots, \boldsymbol{x}_N) = \sum_{i=1}^{p} (\boldsymbol{y}_i - \boldsymbol{h}(\boldsymbol{x}_i, t_i))^{\mathrm{T}} [W] (\boldsymbol{y}_i - \boldsymbol{h}(\boldsymbol{x}_i, t_i)). \tag{19}$$

The quantity $[W]$ is a weighting matrix (typically the inverse of the measurement covariance matrix). The state representation $\boldsymbol{x}_i$ at the measurement epoch $t = t_i$ is required to evaluate Eq. (19). This value can be constructed from a state interpolation in the interval $t_k \leq t_i \leq t_{k+1}$. These expressions are omitted for brevity, but further details are given by Kelly [22].

Given the required constraints and objective, the NLP problem can be summarized as follows

$$\text{minimize} \quad \Phi(\boldsymbol{x}, \ldots, \boldsymbol{x}_N) \quad \text{subject to:} \quad \text{Eq. (16)}. \tag{20}$$

The unknown variables in Eq. (20) are the discretized state vectors at each node $\boldsymbol{x}_1, \boldsymbol{x}_2, \ldots, \boldsymbol{x}_N$. A solution to the NLP problem in Eq. (20) represents a feasible IOD solution that minimizes the weighted sum-square of measurement residuals. The solution remains consistent with system dynamics through enforcement of collocation constraints. However, the stated problem does not account for maneuvers that could be actuated along the trajectory. The following section considers collocation-based IOD with unknown maneuvers.

4.2 Piecewise-Smooth Hermite Transcription with Impulsive Controls

In contrast to short-arc estimation problems, the possibility of an active object performing unknown maneuvers becomes more likely over longer observing gaps. This problem is considered in [13] by appending additional impulsive velocity increments to the defect constraints, while enforcing slack variable constraints to minimize a 1-norm ΔV objective. While this previous approach is sufficient for smaller, station-keeping type maneuvers, it is not resilient to large impulsive velocity increments, such as those actuated by high-thrust chemical propellants.

In this section, we develop a modified maneuver reconstruction method suited to large impulsive maneuvers. The approach requires solving for the velocity increment magnitudes directed along an unknown line of action. First, let us consider the $N-1$ velocity variables $\Delta\boldsymbol{v}_k$ defined at each node as

$$\Delta\boldsymbol{v}_k = w_k \boldsymbol{d}_k, \tag{21}$$

where $w_k \geq 0$ represents the magnitude (or weight) of each velocity increment, and $\boldsymbol{d}_k$ is its corresponding line of action. We define the prior states $\boldsymbol{x}_k^-$ as those without the velocity increment applied, and $\boldsymbol{x}_k^+$ as the post-impulse state at node k. The relationship between these variables is

$$\boldsymbol{x}_k^- = \begin{bmatrix} \boldsymbol{r}_k \\ \boldsymbol{v}_k \end{bmatrix}, \quad \boldsymbol{x}_k^+ = \begin{bmatrix} \boldsymbol{r}_k \\ \boldsymbol{v}_k + \Delta\boldsymbol{v}_k \end{bmatrix}. \tag{22}$$

An illustration of these quantities is shown in Fig. 2. Note that the state interpolant remains continuous between nodes, with discontinuities from velocity increments at each node.

Transcription of the system dynamics is enforced with impulsive velocity increments at collocation points. Hermite basis polynomials are used to approximate the dynamics quadratically, starting from the post-impulse state at node k to the pre-impulse state at node $k+1$. This gives the modified defect constraints from Eq. (16) as

$$\boldsymbol{x}_{k+1}^- - \boldsymbol{x}_k^+ - \frac{1}{6} h_k \left(\boldsymbol{f}_k^+ + 4\boldsymbol{f}_{k+1/2} + \boldsymbol{f}_{k+1}^- \right) = \boldsymbol{0} \quad \text{for} \quad k = 1, \ldots, N-1, \tag{23}$$

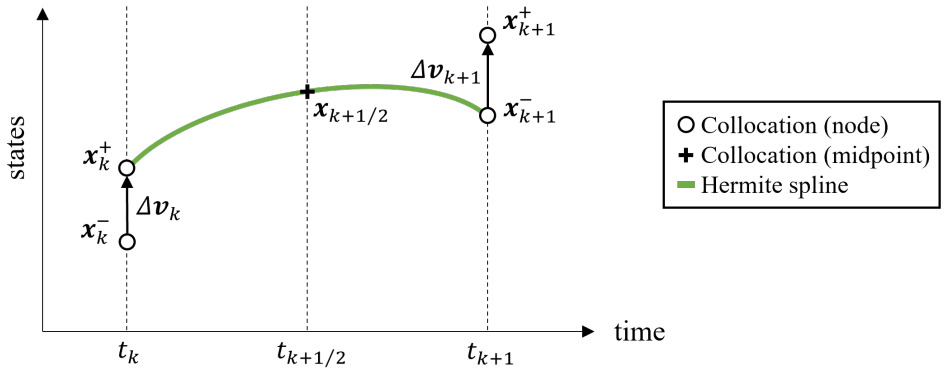

Fig. 2: Hermite-Simpson transcription with impulsive velocity increments at collocation nodes.

where $\boldsymbol{f}_k^+ = \boldsymbol{f}(\boldsymbol{x}_k^+, t_k)$ and $\boldsymbol{f}_{k+1}^- = \boldsymbol{f}(\boldsymbol{x}_{k+1}^-, t_{k+1})$ represent the evaluation of the dynamics function at pre- and post-impulse states, respectively. We also require an expression for the midpoint state under these assumptions. We can construct a state interpolant (see Eq. (27)) evaluated at time $t_{k+1/2}$, giving the following:

$$\boldsymbol{x}_{k+1/2} = \frac{1}{2}(\boldsymbol{x}_k^+ + \boldsymbol{x}_{k+1}^-) + \frac{h_k}{8}(\boldsymbol{f}_k^+ - \boldsymbol{f}_{k+1}^-). \tag{24}$$

Equations (23) and (24) incorporate the $\Delta\boldsymbol{v}$ control variables through the post-impulse state $\boldsymbol{x}_k^+$. However, in contrast to the methodology in [13], the defect constraints also require an extra evaluation of the system dynamics at node $k+1$ to ensure the Hermite interpolation is smooth between impulsive velocity jumps.

Next, to ensure an IOD solution is consistent with observed measurements, we enforce a residual constraint of the form:

$$\boldsymbol{y}_i - \boldsymbol{h}(\boldsymbol{x}_i, t_i) = \boldsymbol{0} \quad \text{for} \quad i = 1, \ldots, p. \tag{25}$$

This expression is functionally similar to the objective in Eq. (19) which minimizes the weighted sum of measurement residuals, but by construction the constraint in Eq. (25) must be precisely satisfied on a feasible trajectory. We must also account for the case when measurement times $t_k < t_i < t_{k+1}$ do not coincide with the mesh times. A state interpolant consistent with the collocation method (see [22]) is constructed to solve this problem. A quadratic spline representation of the state derivative between the pre- and post-impulse velocity increments is

$$\frac{\mathrm{d}\boldsymbol{x}(\tau)}{\mathrm{d}\tau} \approx \boldsymbol{f}_k^+ + \left(-3\boldsymbol{f}_k^+ + 4\boldsymbol{f}_{k+1/2} - \boldsymbol{f}_{k+1}^-\right)\left(\frac{\tau}{h_k}\right) + \left(2\boldsymbol{f}_k^+ - 4\boldsymbol{f}_{k+1/2} + 2\boldsymbol{f}_{k+1}^-\right)\left(\frac{\tau}{h_k}\right)^2, \tag{26}$$

where $\tau = t - t_k$ is the time increment from the neighboring node k. Integrating this expression once with respect to τ with the boundary condition $\boldsymbol{x}(0) = \boldsymbol{x}_k^+$ gives a state interpolant for time between nodes k and $k+1$:

$$\boldsymbol{x}(\tau) = \boldsymbol{x}_k^+ + \boldsymbol{f}_k^+\tau + \frac{1}{2h_k}\left(-3\boldsymbol{f}_k^+ + 4\boldsymbol{f}_{k+1/2} - \boldsymbol{f}_{k+1}^-\right)\tau^2 + \frac{1}{3h_k^2}\left(2\boldsymbol{f}_k^+ - 4\boldsymbol{f}_{k+1/2} + 2\boldsymbol{f}_{k+1}^-\right)\tau^3. \tag{27}$$

Note that, through incorporation of the post-impulse velocity variables at node k, Eq. (27) is influenced by the velocity control variables. This means that the measurement function evaluated at interpolated epochs depends on both state and control variables, even though the measurement model itself only depends on states.

Now, in order to properly account for the weights of each $\Delta\boldsymbol{v}_k$, the direction vectors must be normalized to unit magnitude. Two approaches are possible. The first is to simply divide Eq. (21) by the magnitude $\|\boldsymbol{d}_k\|$ to normalize the direction vectors. However, this has the effect of introducing a singularity near zero values, which can cause poor conditioning of the constraint Jacobian. Instead, we restrict the direction vector magnitudes using additional NLP constraints of the form

$$\boldsymbol{d}_k^{\mathrm{T}}\boldsymbol{d}_k - 1 = 0 \quad \text{for} \quad k = 1, \ldots, N-1. \tag{28}$$

Enforcing the constraints in Eq. (28) allows the solver to fully explore the solution space without encountering singularities or divide-by-zero errors. Control magnitudes of zero are supported by setting $w_k = 0$. The tradeoff for this approach is that it requires an additional $N-1$ constraints in the NLP problem structure.

A side effect of including the impulsive velocity variables is the NLP solver may compensate for dynamic mismodeling (i.e., transcription errors) using excess control effort. However, to prevent each velocity impulse from growing unchecked, we minimize the sum of control magnitudes $\|\Delta \boldsymbol{v}_k\|$ across the trajectory. The minimum control magnitude objective is then stated as

$$\Phi(w_1, \ldots, w_{N-1}) = \sum_{k=1}^{N-1} w_k. \tag{29}$$

Some useful observations can be made regarding this objective structure. First, the direction vectors do not appear in Eq. (29), meaning the gradient with respect to these quantities is zero. However, the direction vectors are required to enforce collocation constraints in Eq. (23), so their influence on the problem structure is still seen indirectly. Second, the weights w_k can be constrained as NLP decision variables, allowing the user to set an upper bound on the velocity increments at collocation points. This feature can be used to enforce realistic thrust performance limits on the controls.

Given the objective and constraints, the collocation-based IOD method with impulsive control reconstruction is given by the following NLP problem

$$\text{minimize} \quad \Phi(w_1, \ldots, w_{N-1}) \quad \text{subject to:} \quad \text{Eqs. (23), (25), and (28).} \tag{30}$$

The unknown variables for this problem include: the discretized pre-impulse state vectors at each node $\boldsymbol{x}_1^-, \boldsymbol{x}_2^-, \ldots, \boldsymbol{x}_N^-$, the velocity impulse direction vectors $\boldsymbol{d}_1, \ldots, \boldsymbol{d}_{N-1}$, and the velocity impulse magnitudes $w_1, w_2, \ldots, w_{N-1}$. Equation (30) represents a discrete representation of the IOD problem with impulsive control inputs at each node. The objective minimizes the sum of vector magnitudes of velocity increments, which reflects typical spacecraft maneuvers that attempt to minimize fuel expenditure.

4.3 NLP Gradient and Sparsity Structure

The NLP structures in Eqs (20) and (30) can be solved with efficient interior-point algorithms such IPOPT [23] and SNOPT [24]. These algorithms usually require derivative information in order to compute Newton search directions, including the objective gradient and the constraint Jacobian. These quantities are briefly outlined below to inform implementation of the approach.

The objective in Eq. (29) is a linear function of the velocity impulse weights w_k only. Therefore, the objective gradient with respect to the unknown parameters can be easily found based on the following information:

$$\frac{\partial \Phi}{\partial \boldsymbol{x}_k^-} = \boldsymbol{0}^{\mathrm{T}}, \quad \frac{\partial \Phi}{\partial \boldsymbol{d}_k} = \boldsymbol{0}^{\mathrm{T}}, \quad \frac{\partial \Phi}{\partial w_k} = 1. \tag{31}$$

These expressions allow the user to construct the appropriate gradient vector, which is a constant vector independent of the state and velocity control variables.

Similarly, we also require expressions for the constraint Jacobian. These expressions can be found in closed form due to the use of analytic dynamics and constraints in the preceding sections (see Appendix A). In addition, the sparsity structure of the constraint Jacobian is needed to inform search direction computation in the NLP solver. This sparsity structure for the constraints in Eq. (30) is shown in Fig. 3. Non-zero entries of the matrix are denoted by X's, and empty blocks are left blank. This information can improve overall solution speed and convergence of the NLP solver.

4.4 Error Analysis

It is helpful to evaluate a solution between nodes in order to quantify integration accuracy everywhere in a trajectory. The corresponding transcription errors quantify how well a final solution satisfies integration constraints. For a feasible solution, errors at collocation points will be satisfied within solver tolerances. Between node times, the solution error can be computed as

$$\boldsymbol{\varepsilon}(t) = \dot{\boldsymbol{x}}(t) - \boldsymbol{f}(\boldsymbol{x}(t), t), \tag{32}$$

where $\dot{\boldsymbol{x}}(t)$ and $\boldsymbol{x}(t)$ are evaluated with the piecewise continuous interpolation expressions in Eqs. (26) and (27), respectively. We can verify the error at collocation points is driven to zero when the condition in Eq. (23) is exactly met. Evaluating Eq. (27) at time $t = t_k$ gives

$$\boldsymbol{\varepsilon}(t_k) = \boldsymbol{f}_k^+ - \boldsymbol{f}(\boldsymbol{x}_k^+, t_k) = \boldsymbol{0}. \tag{33}$$

	Node	$\boldsymbol{x}_1^-$	$\boldsymbol{x}_2^-$	$\cdots$	$\boldsymbol{x}_N^-$	$\boldsymbol{d}_1$	$\cdots$	$\boldsymbol{d}_{N-1}$	w_1	$\cdots$	w_{N-1}
Eq. (23)	1	X	X			X			X		
	$\vdots$		$\ddots$	$\ddots$			$\ddots$			$\ddots$	
	$N-1$			X	X			X			X
Eq. (25)	1	X	X			X			X		
	$\vdots$		$\ddots$	$\ddots$			$\ddots$			$\ddots$	
	$N-1$			X	X			X			X
Eq. (28)	1					X					
	$\vdots$						$\ddots$				
	$N-1$							X			

Fig. 3: NLP constraint Jacobian sparsity structure.

At the midpoint and endpoint of the interval, the solution depends on the defect constraint in Eq. (23). In general, the constraint residual will be satisfied to within some small, non-zero error $\boldsymbol{e}_k$ relative to the solver tolerance. After some simplification, we find

$$\boldsymbol{\varepsilon}(t_{k+1/2}) = \boldsymbol{f}_{k+1/2} - \boldsymbol{f}\left(\boldsymbol{x}_{k+1/2} - \frac{1}{2}\boldsymbol{e}_k, t_{k+1/2}\right), \tag{34a}$$

$$\boldsymbol{\varepsilon}(t_{k+1}) = \boldsymbol{f}_{k+1}^- - \boldsymbol{f}\left(\boldsymbol{x}_{k+1}^- - \boldsymbol{e}_k, t_{k+1}\right). \tag{34b}$$

By virtue of Eq. (33), transcription errors are expected to be numerically zero (within floating point precision) at the start of the interval, regardless of the solver convergence tolerance. For the endpoint of the interval, we can approximate errors at time with a Taylor series centered at $\boldsymbol{x}_{k+1}^-$:

$$\boldsymbol{\varepsilon}(t_{k+1}) = \boldsymbol{f}_{k+1}^- - \left[\boldsymbol{f}\left(\boldsymbol{x}_{k+1}^-, t_{k+1}\right) - \left.\frac{\partial \boldsymbol{f}}{\partial \boldsymbol{x}}\right|_{\boldsymbol{x}_{k+1}^-} \cdot \boldsymbol{e}_k + \mathscr{O}\left(\|\boldsymbol{e}_k\|^2\right)\right]. \tag{35}$$

For an assumed small $\boldsymbol{e}_k$, higher order terms are truncated to give an estimate for the endpoint errors

$$\boldsymbol{\varepsilon}(t_{k+1}) \approx \left(\frac{\partial \boldsymbol{f}_{k+1}^-}{\partial \boldsymbol{x}_{k+1}^-}\right)\boldsymbol{e}_k. \tag{36}$$

Similarly, at the midpoint of an interval it follows that

$$\boldsymbol{\varepsilon}(t_{k+1/2}) \approx \frac{1}{2}\left(\frac{\partial \boldsymbol{f}_{k+1/2}}{\partial \boldsymbol{x}_{k+1/2}}\right)\boldsymbol{e}_k. \tag{37}$$

Equations (36) and (37) give a direct mapping between NLP constraint residuals and the corresponding transcription errors. To first order, transcription errors are scaled linearly by the local dynamics jacobian. These expressions allow us to examine the dynamical consistency of intermediate solutions to identify areas where transcription errors are present. Transcription errors at the midpoint and endpoint can also be bounded in each interval relative to the solver tolerances. A depiction of these error metrics is shown in Fig. 4.

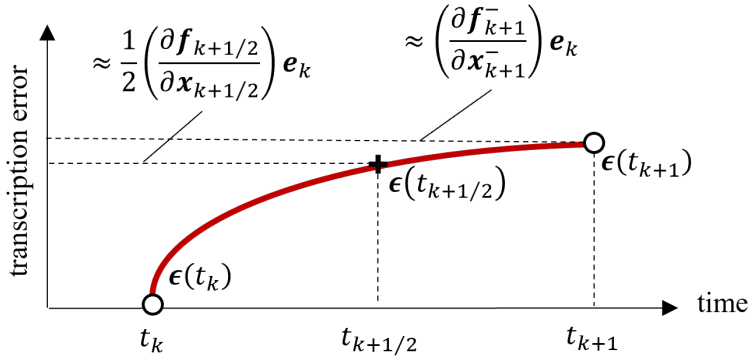

Fig. 4: Transcription error and NLP constraint feasibility evaluated at the endpoints and midpoint of a discretized solution interval.

5. RESULTS

This section outlines two example applications for the preceding IOD algorithm development. Rotating frame dynamics derived from SPICE data allow for precise modeling of realistic spacecraft trajectories under the influence of multiple gravitational bodies. These dynamics are applied to the collocation-based IOD methods outlined in the preceding section. By incorporating the high-fidelity ephemeris models, we reduce the likelihood of overestimating maneuvers due to dynamic mismodeling.

The following examples demonstrate these methods with realistic IOD scenarios using archival data from the NASA JPL Horizons system. The coordinate center is set as the Earth-Moon barycenter with quantities expressed in ICRF coordinates. The reference plane is defined by the equatorial x-y axes of the reference frame using geometric states without stellar aberration correction. The generated time series data are considered the reference truth values for simulated optical angles measurements. The observer location is assumed as Boulder, CO ($-105.280°$W, $40.013°$N). For the purposes of demonstration, we do not consider target apparent magnitudes or viewing geometries when generating measurements for IOD; operational applications of these methods would parse measurements accordingly based on available sensors and observability.

5.1 Non-maneuvering IOD: TESS

We first consider a non-maneuvering case from the Transiting Exoplanet Survey Satellite (TESS). The primary mission for TESS ended on July 4, 2020, which consisted of a two-year wide field imaging campaign to detect planetary transits [25]. The TESS mission is in its extended phase, and as such is less likely to make large maneuvers or adjustments to its primary orbit. A time window of 2024 Nov 21 12:00:00 to 2024 Dec 4 16:00:00 TBD is chosen to cover approximately one orbit period of TESS. Optical angles measurements are simulated from a ground-based observer in Boulder, CO using the `IAU_EARTH` model in SPICE. A sequence of six angles-only measurements are simulated with equal spacing across the observing window. Parameter bounds and initial guesses for NLP parameters are given in Table 3. A generic initial guess at the L_1 Earth-Moon Lagrange point is assumed, reflecting the fact that IOD applications have little to no initial state knowledge of a target.

Table 3: NLP parameter bounds and initial guesses for TESS example. Quantities are expressed in terms of non-dimensional distances (DU) and time units (TU).

Parameter	Lower Bound	Upper Bound	Initial Guess
$\boldsymbol{x}_k^-$	$[0,-1,-1,-2,-2,-2]^{\mathrm{T}}$	$[1.5,1,1,2,2,2]^{\mathrm{T}}$	L_1

The NLP structure in Eq. (20) is applied to the TESS example. No maneuvers are reconstructed, instead minimizing a weighted sum of measurement residuals at each observation epoch with assumed ballistic motion. The SPICE-derived equations of motion in Eq. (7) are applied in the EM rotating frame. The collocation-based IOD solution is shown

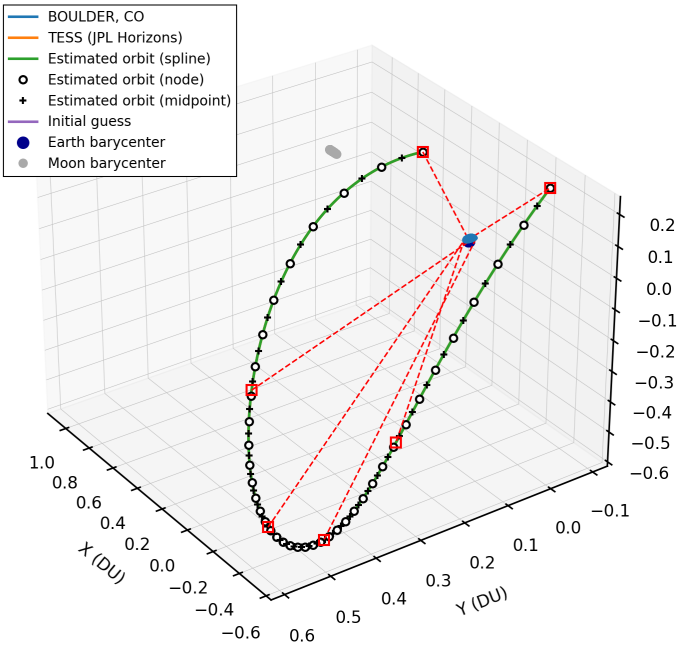

Fig. 5: Reconstructed TESS trajectory from IOD solution in EM rotating frame.

Table 4: Initial conditions for TESS at epoch 2024 Nov 21 12:00:00 TDB.

State	Value
X	-7.40820968E+04 km
Y	2.53215225E+04 km
Z	1.07233663E+05 km
$\dot{X}$	-7.9713205E-01 km/s
$\dot{Y}$	-1.82214319E+00 km/s
$\dot{Z}$	-3.86606211E-01 km/s

in Fig. 5. The Earth and Moon barycenter locations from SPICE are also plotted at mesh times for reference. The estimated IOD solution is plotted at mesh nodes and midpoints, along with a continuous spline interpolation of the solution. Table 4 lists initial conditions at epoch in the J2000 inertial frame. We emphasize that these initial conditions are not used to propagate the truth states, which are sourced from JPL Horizons to eliminate possible sources of error. Fig. 5 shows good agreement between simulated and truth data for TESS. A solution is found starting from a poor initial guess at the Earth-Moon L_1 Lagrange point.

We further investigate the solution accuracy in Fig. 6. In Fig. 6a, collocation errors are plotted as a function of node location in the transcription scheme. The errors at the start of each interval are zero to within machine precision, which is expected from the error analysis in Eq. (33). Errors at the midpoints are also low, since collocation conditions are applied at the midpoint of each interval with Hermite polynomials. It is also helpful to evaluate the interpolated state error between nodes, as this quantifies the overall integration accuracy and non-node times. The interpolated errors increase to about 10^{-2}, which indicates moderately low integration errors. This effect is exaggerated near the endpoints of the solution, which is explained by the fact that these points are near perigee where the dynamics are changing more quickly (and less closely approximated by cubic polynomials). For the purposes of this demonstration, errors were sufficiently low with a uniform node spacing, although mesh refinement [26] could further increase the solution accuracy.

The NLP objective and problem feasibility are shown in Fig. 6b. The initial guess begins with a poor objective value and feasibility, as the theoretical L_1 Earth-Moon Lagrange point is not dynamically consistent in an ephemeris model. The solver makes good progress from this initial guess, driving the primal and dual problem infeasibility below desired tolerances. The objective function also shows consistent improvement with each iteration. These results indicate that the predicted solution is a local optimum that satisfies integration constraints. Errors in position and velocity magnitudes compared to JPL Horizons data are given in Fig. 6c. Position errors are on the order of 20 km and velocity errors are below 0.5 m/s. These values are useful to give an intuitive measure of overall solution accuracy. As discussed previously, errors are higher near perigee, which is expected due to the fixed integration step size within the transcription scheme. Results for the TESS example show the collocation-based IOD method aligns with truth data when using SPICE-derived rotating frame dynamics.

Trends of individual state coordinates are given in Fig. 8. Plots of the collocation-based IOD solution along with the

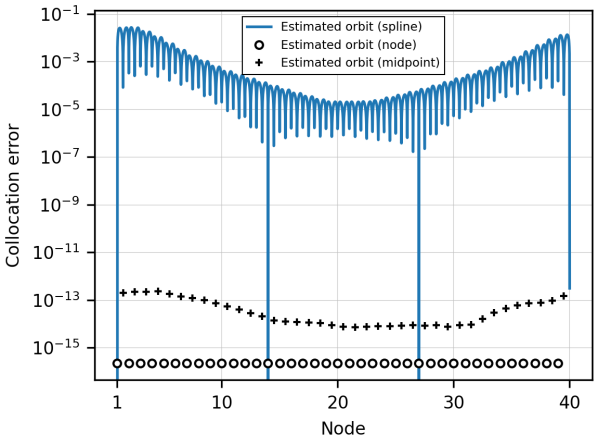

(a) Collocation residuals for Hermite-Simpson integration

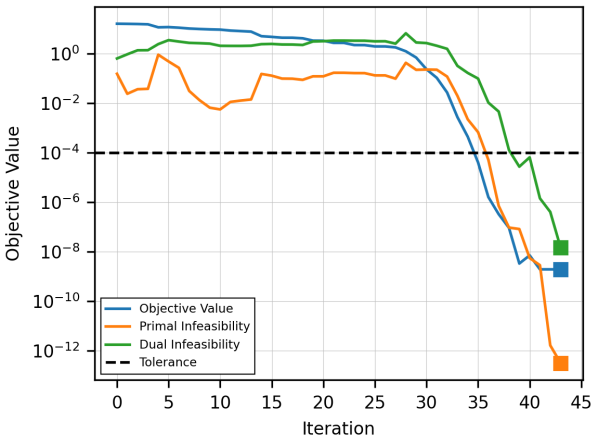

(b) NLP objective and feasibility versus solver iterations

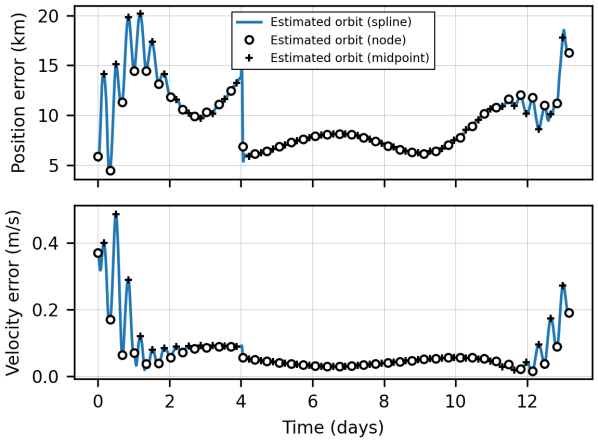

(c) Errors in position and velocity compared to JPL Horizons data

Fig. 6: Collocation errors, feasibility, and solution accuracy for TESS example.

truth data are given. Observation epochs are marked by red squares. The upper and lower bounds in Table 5 are clearly adequate to fully enclose the TESS trajectory. Exact solver bounds may not always be known a priori, but they can be roughly chosen based on domain of application and expected orbits. The corresponding measurement quantities are shown in Fig. 7. Although angles-only measurements are used in this example, the angle rates are also shown for reference. It is also important to note that measured angle quantities in Fig. 7a are defined with respect to the EM rotating frame, which are derived from inertial RA and DEC angles. Trends in both angles and angle rates follow expected truth values. Oscillations in Fig. 7b arise from the non-zero inclination of the observer relative to the lunar orbital plane.

Parameters from the NLP solver are summarized in Table 5. A solution is found in 43 iterations, taking less than one second of CPU time. The overall NLP error is also low, indicating a local minimum was found by the solver. These results are useful to evaluate the overall solution progress and convergence. This example demonstrates application of a non-maneuvering IOD problem to the SPICE rotating frame dynamics in preceding sections. In the following example, we consider a case with documented maneuvers for application of the impulsive IOD strategy.

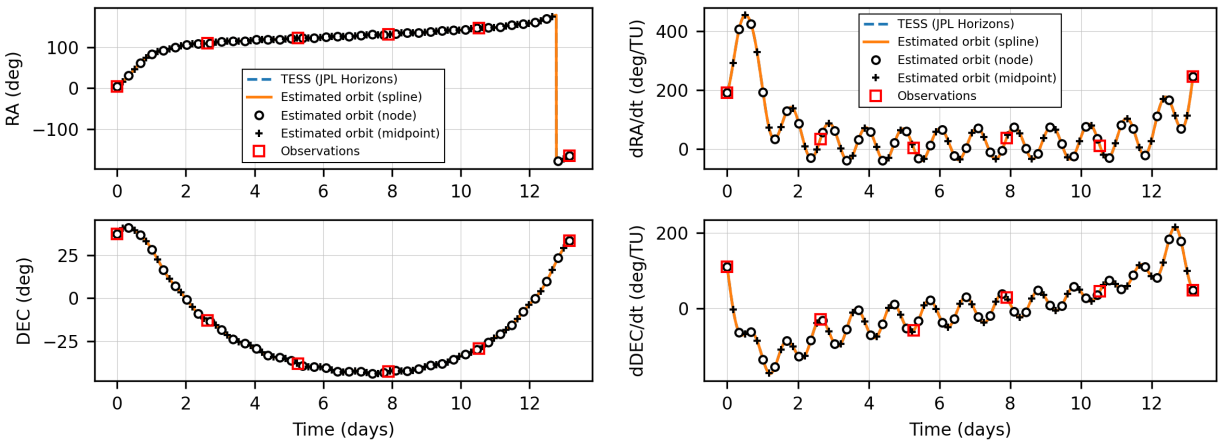

(a) Reconstructed RA and DEC angles versus time

(b) Reconstructed angle rates versus time

Fig. 7: Optical angles measurements for TESS example.

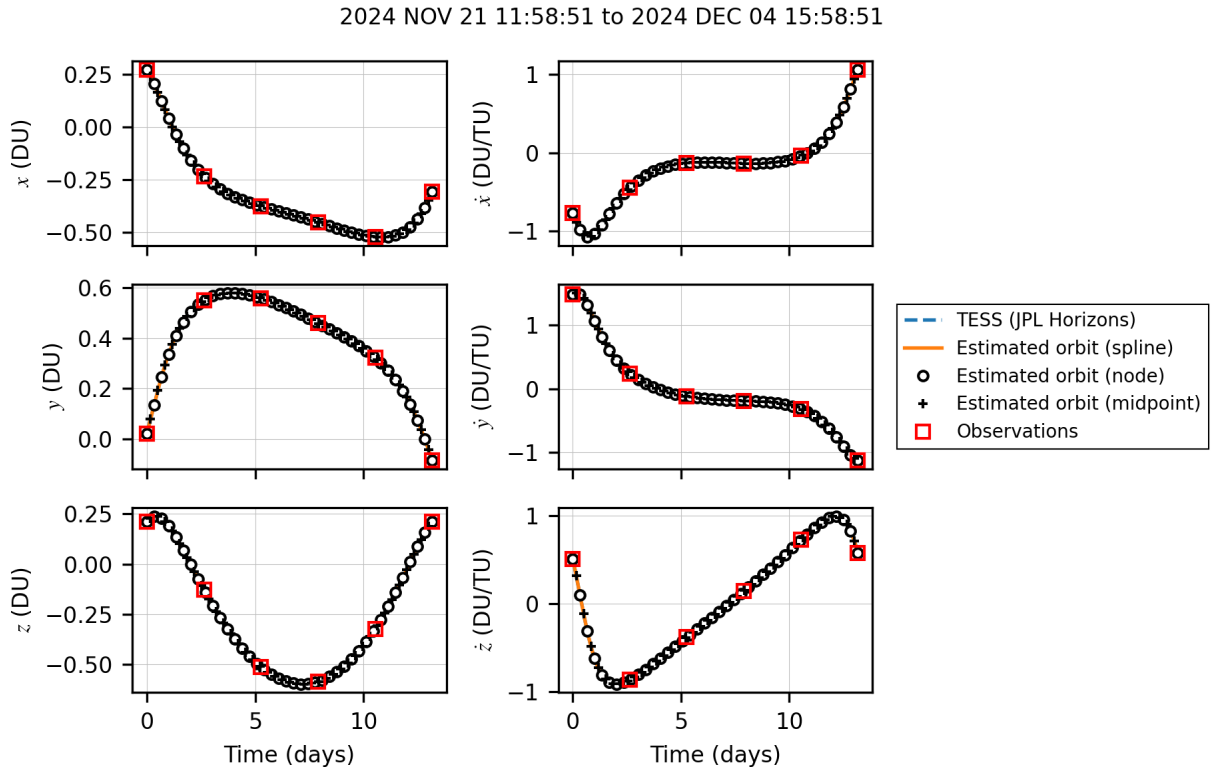

Fig. 8: Position and velocity states in EM rotating frame compared to JPL Horizons reference data for TESS example.

Table 5: NLP solver accuracy and convergence criteria for TESS example.

Parameter	Value
Nodes	40
Free variables	240
Constraints	234
Iterations	43
CPU time (s)	0.773
NLP Error	4.750e-09

5.2 IOD with Near-Impulsive Maneuver: Artemis I

In the next example, we apply the collocation-based IOD approach to a maneuvering observation scenario. The Artemis I mission launched on Nov 16, 2022 with the primary objective of testing the readiness of the Orion capsule for manned missions [27]. The Artemis I capsule entered a distant retrograde orbit (DRO) about the moon on Nov 25, 2022 following an outbound powered flyby and DRO insertion (DRI) burn. The DRO phase lasted six days before a DRO departure (DRD) burn and return powered flyby put the spacecraft on a direct Earth entry return path. The Artemis I mission is a compelling example for application of IOD with impulsive maneuvers. Published maneuver timings and magnitudes from the Artemis I mission [28] allow for direct comparison to post-flight data.

The Artemis I mission is chosen for study between epochs 2022 Nov 26 00:00:00 and 2022 Dec 1 21:00:00 TDB, capturing the DRO phase between DRI and DRD burns. Two known trajectory correction maneuvers, OM-1 and OM-3, were actuated during this time span (OM-2 was not performed). For this example, we consider data sourced from the JPL Horizons system for the Artemis I spacecraft between these chosen epochs. Simulated angle and angle rates optical observations are generated using this data as the reference truth state of the spacecraft. These observations are used for application of the collocation-based IOD method with impulsive maneuver estimation. The resulting maneuvers can then be compared to published data. We note that, although the maneuver time is tied to the collocation mesh spacing, the number and magnitude of burns is not predetermined. Instead, the solver is tasked with finding the optimal combination of impulsive velocity increments that produce the minimum total ΔV across the observing window.

NLP solver bounds and initial guess values are shown in Table 6. In contrast to Table 5, this example includes the additional unknown velocity impulse direction vectors and weights as unknown parameters. No upper bound is enforced on the maneuver magnitudes, although this upper bound could be included based on assumed capabilities of a spacecraft using chemical propellant thrust. The initial guess for this example is the L_2 Lagrange point. Although this point is a theoretical result of CR3BP motion, it does not exist in the full ephemeris model. However, this initial guess is sufficient for seeding the IOD algorithm. The J2000 state for Artemis I at initial epoch is given in Table 7.

Table 6: NLP parameter bounds and initial guesses for Artemis I example. Quantities are expressed in terms of non-dimensional distances (DU) and time units (TU).

Parameter	Lower Bound	Upper Bound	Initial Guess
$\boldsymbol{x}_k^-$	$[0.5,-0.5,-0.5,-2,-2,-2]^{\mathrm{T}}$	$[1.5,0.5,0.5,2,2,2]^{\mathrm{T}}$	L_2
$\boldsymbol{d}_k$	$[-1,-1,-1]^{\mathrm{T}}$	$[1,1,1]^{\mathrm{T}}$	$[0,0,0]^{\mathrm{T}}$
w_k	0	N/A	0

The reconstructed IOD solution is shown in Fig. 9. This figure illustrates the observation and trajectory geometry in the inertial frame. Observations are constrained by a lunar exclusion zone defined by a 5° cone angle, due to limitations of imaging dim objects near the illuminated lunar disk. A total of six angles and angle rates observations are used, taking into account the exclusion zone.

A quantitative look at this data can be found in Fig. 10, starting with the overall integration accuracy indicated in Fig. 10a. Errors at collocation nodes are zero to within floating point precision. The magnitude of integration errors is evaluated between nodes, as well as at the midpoint of each interval. These errors are sufficiently low (less than 10^{-4}), indicating the resulting solution satisfies integration constraints. Fig. 10b shows the NLP solver feasibility and objective value. The primal infeasibility is below the specified tolerance, indicating the solver constraints are acceptable. The dual infeasibility is above this threshold, but the NLP solver is able to determine an acceptable solution based on optimality criteria. The objective value consists of minimizing the sum magnitude of impulsive

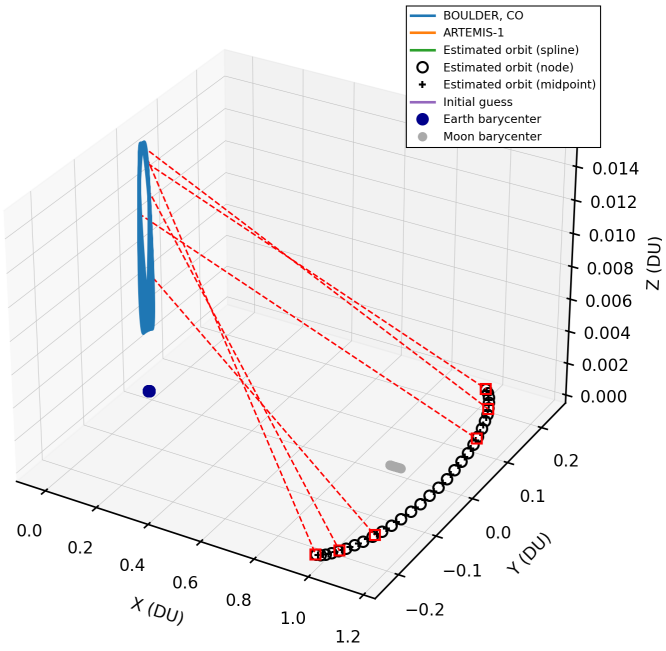

Fig. 9: Reconstructed IOD solution for Artemis I in EM rotating frame coordinates. The shaded region represents a 5° lunar exclusion zone for optical observations.

Table 7: Initial conditions for Artemis I at epoch 2022 Nov 25 22:00:00 TDB.

State	Value
X	9.31886574e+04 km
Y	-3.29045779e+05 km
Z	-1.76273686e+05 km
$\dot{X}$	9.84129774e-01 km/s
$\dot{Y}$	-5.90153790e-02 km/s
$\dot{Z}$	-9.94359228e-02 km/s

control inputs, and is thus not considered relative to a specified solver tolerance. These values indicate the resulting solution is a local minimum of the NLP problem. The relative position and velocity errors are shown in Fig. 10c. In contrast to Fig. 10a, which indicates integration errors inherent to fixed step-size implicit integrators, Fig. 10c shows errors relative to the truth states from JPL Horizons data. Position and velocity errors at mesh points are on the order of 100 km and 1 m/s, respectively. A spike in velocity error appears between nodes at approximately 2.5 days. This velocity error does not correlate to any published maneuvers during this time, but may be due to the transition between concatenated post-launch trajectory data from NASA JSC. A second spike near 5 days coincides with the OM-3 maneuver time, which is explained by the slight offset of the true maneuver time from the collocation mesh spacing.

Reconstructed angles and angle rates are given in Fig. 11. For this example, both angles and rates quantities were used as measurement constraints in Eq. (25). Trends in RA and DEC angles match well with expected truth values, both at and between measurement epochs indicated by red squares. Note that, as with the previous example, angles quantities are defined with respect to the EM rotating coordinate frame. These trends illustrate the time-varying behavior of angles quantities after a full trajectory is reconstructed from measurements. The individual state variables as a function of time are shown in Fig. 12. Trends in the position and velocity state variables are plotted, in addition to the observation epochs and truth values from JPL Horizons data. A small spike in the z component of velocity is visible at approximately 2.5 days, which is the same anomaly discussed in Fig. 10c. The states otherwise show good agreement with expected truth values across the full reconstructed trajectory.

The control history for Artemis I is shown in Fig. 13. Impulsive controls from the IOD solution are shown as stem plots. For the epochs between the DRI and DRD burns, two known trajectory maneuvers were actuated by ARTEMIS flight controllers [28]. These burns are indicated by solid vertical lines. The OM-1 burn took place at 2022 Nov 26 21:52:28 UTC, about one day after initial epoch in Fig. 13. Post-flight review quantified this burn at 0.05 ft/s. The reconstructed controls corresponding to the OM-1 epoch show a small burn of 0.20 m/s (0.65 ft/s) near this time. While this over-predicts the true maneuver magnitude, it does indicate a small maneuver is detected near the OM-1 epoch. The OM-3 maneuver was actuated at 2022 Nov 30 21:53:56 UTC with a post-flight review magnitude of 43.37 ft/s. The reconstructed control solution nearest to this epoch is 14.72 m/s (48.29 ft/s), corresponding to 11% error. These results

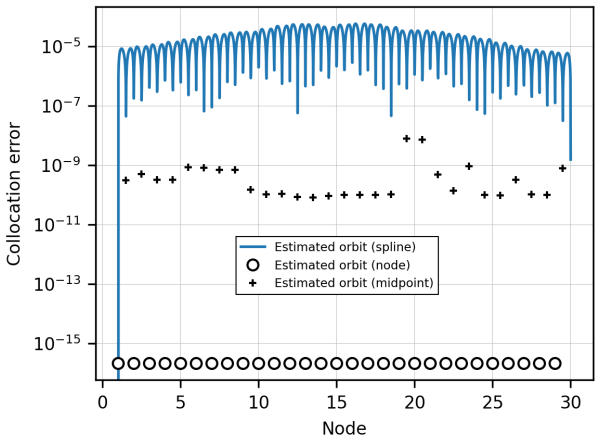

(a) Collocation residuals for Hermite-Simpson integration

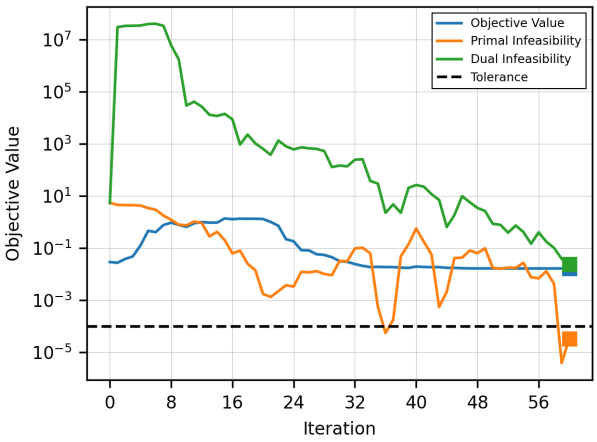

(b) NLP objective value and feasibility

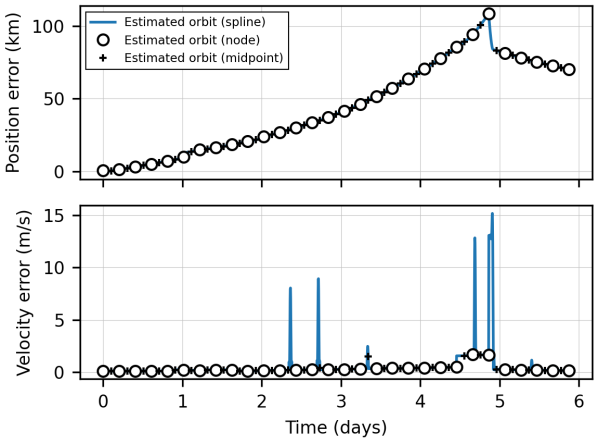

(c) Errors in position and velocity compared to JPL Horizons data

Fig. 10: Collocation errors, feasibility, and solution accuracy for Artemis I example.

indicate that impulsive velocity-based control inputs for Artemis I are successfully reconstructed in the IOD algorithm from optical angles measurements.

NLP solver iterations and accuracy are summarized in Table 8. The total number of free variables and constraints is larger than in Table 5, which is expected because of the additional velocity direction and magnitude variables included as NLP parameters. The number of constraints is also higher due to the inclusion of angle rates measurements in this example (as opposed to angles-only measurements). A single-threaded solution converges in 60 iterations, taking about one second of CPU time. This rapid convergence property is useful for real-time applications, as it enables fast orbit determination with minimal computational overhead.

The Artemis I example demonstrates IOD with impulsive maneuvers. As indicated in Table 6, the initial guess is coincident with the Earth-Moon L_2 Lagrange point, which is straightforward to compute. No upper bounds on the velocity impulse magnitudes are required, although these bounds could be included based on known performance or thrust limits of a target. Results are supported by quantifying NLP solver feasibility and convergence behavior, indicating that the solution is a local minimum that satisfies integration and measurement c onstraints. Finally, trends in the reconstructed state solution at and between mesh times are measured against data from the JPL Horizons system to validate results.

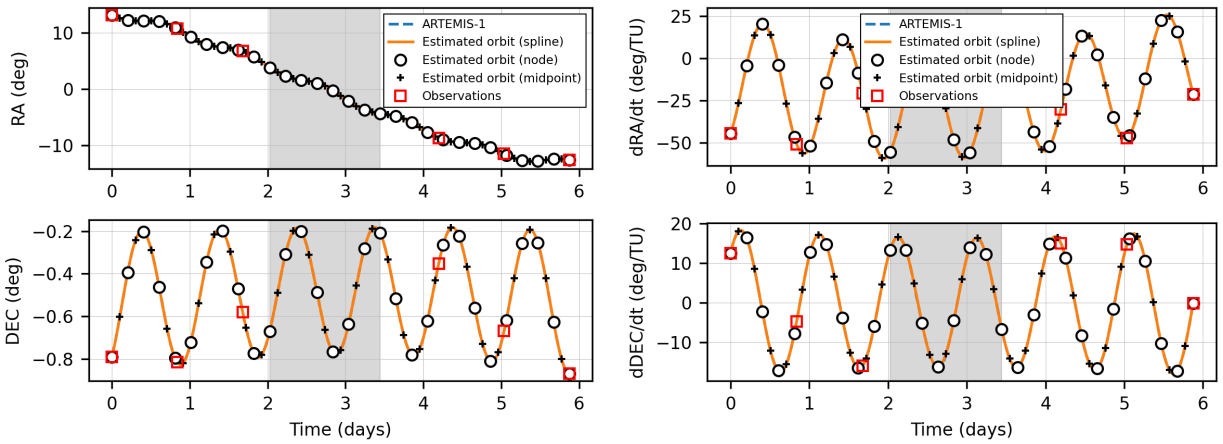

(a) Angles (b) Angle rates

Fig. 11: Reconstructed angles and angle rates versus time for Artemis I example.

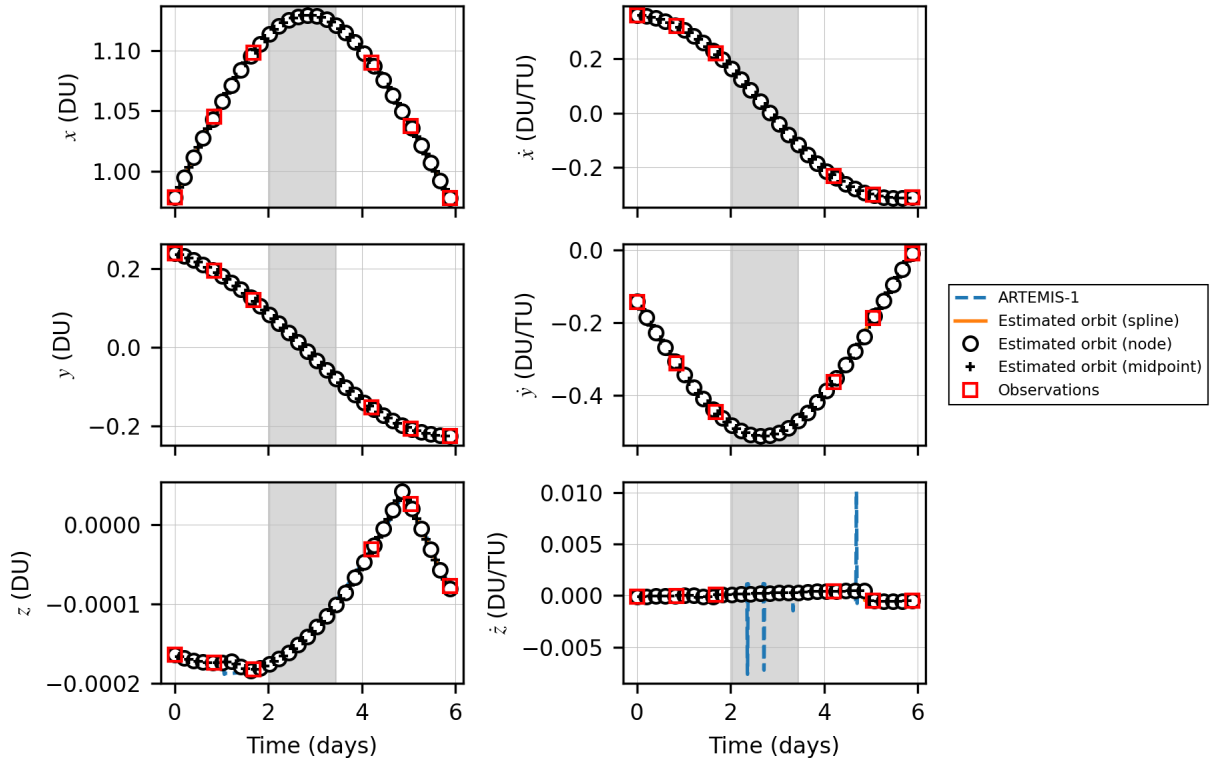

Fig. 12: Position and velocity state components compared to JPL Horizons data for Artemis I example.

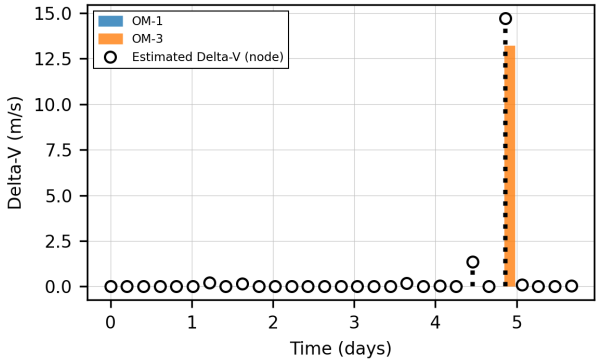

Fig. 13: Reconstructed impulsive control inputs versus time. Estimated maneuvers are compared to published Artemis I post-flight data [28].

Table 8: NLP solver accuracy and convergence criteria for Artemis I example.

Parameter	Value
Nodes	30
Free variables	296
Constraints	239
Iterations	60
CPU time (s)	1.172
NLP Error	5.438e-05

6. CONCLUSIONS

A robust and accurate collocation-based IOD algorithm is developed using SPICE ephemeris data. A general rotating frame definition is given, and an exact dynamical description of motion is derived. No assumptions for elliptical or co-planar orbits are assumed, and quantities can be obtained directly from SPICE for accurate dynamics modeling. The ephemeris model is incorporated into a collocation-based IOD method to enable implicit integration of high-fidelity system dynamics. Application to non-maneuvering spacecraft is shown and compared to truth data from the NASA JPL Horizons system. The approach is then extended to include impulsive velocity control estimation. A Hermite spline interpolation is modified to account for the pre- and post-control states while retaining differentiable functions. The resulting problem structure is discussed and applied to an active spacecraft tracking problem. Reconstructed states and maneuvers are compared to published post-flight data. Results show close agreement with reference data, indicating the method can find accurate solutions to IOD problems with unknown maneuvers. These capabilities can greatly enhance SSA operations by informing detection and tracking of active spacecraft in the cislunar regime.

ACKNOWLEDGEMENTS

Support for this research was provided through an AFRL Cooperative Agreement (award No. FA9453-22-2-0050) at the University of Colorado Boulder.

REFERENCES

[1] Pedro R Escobal. *Methods of Orbit Determination*. Robert E. Krieger Publishing Company, Malabar, FL, 1985.
[2] Sajjad Kazemi, Nasser L Azad, K Andrea Scott, Haroon B Oqab, and George B Dietrich. Orbit determination for space situational awareness: A survey. *Acta Astronautica*, 2024.
[3] Andrea Scorsoglio, Andrea D'Ambrosio, Luca Ghilardi, Roberto Furfaro, and Vishnu Reddy. Physics-Informed Orbit Determination For Cislunar Space Applications. In *Advanced Maui Optical and Space Surveillance*

(AMOS) Technologies Conference, 2023.

[4] Gregory Badura, Miguel Velez-Reyes, Brian Gunter, Christopher Valenta, and Koki Ho. Regularizing Training of Physics Informed Neural Networks (PINNs) for Cislunar Orbit Determination via Transfer Learning. In *Advanced Maui Optical and Space Surveillance Technologies (AMOS) Conference*, 2024.

[5] Alexander Cabello, Jeff Houchard, Cameron Harris, J Zachary Gazak, Jonathan Kadan, and Justin Fletcher. Learned Initial Orbit Determination from Simulated Electro-Optical Observations. In *Advanced Maui Optical and Space Surveillance (AMOS) Technologies Conference*, page 75, 2024.

[6] J Ojeda Romero, W Schlei, G Whipps, N LaFarge, G Fritsch, and S Phillips. An Adaptive Approach to the Initial Orbit Determination Problem in the Cislunar Regime Using Machine Learning. In *Advanced Maui Optical and Space Surveillance (AMOS) Technologies Conference*, page 63, 2024.

[7] Mark Bolden, I Hussein, H Borowski, R See, and E Griggs. Probabilistic initial orbit determination and object tracking in cislunar space using optical sensors. In *Advanced Maui Optical and Space Surveillance Technologies (AMOS) Conference*, 2022.

[8] C Channing Chow, Charles J Wetterer, Jason Baldwin, Micah Dilley, Keric Hill, Paul Billings, and James Frith. Cislunar Orbit Determination Behavior: Processing Observations Of Periodic Orbits with Gaussian Mixture Model Estimation Filters. *The Journal of the Astronautical Sciences*, 69(5):1477–1492, 2022.

[9] Trevor N Wolf and Brandon A Jones. Intelligent Sensor Tasking for Minimum Time Space Object Acquisition. In *Advanced Maui Optical and Space Surveillance Technologies Conference, AMOS, Maui, Hawaii, USA*, 2023.

[10] Samuel Wishnek, Marcus J Holzinger, and Patrick Handley. Robust Cislunar Initial Orbit Determination. In *Advanced Maui Optical and Space Surveillance Technologies (AMOS) Conference*, 2021.

[11] J Gaebler, K Hill, C Wetterer, and J Bruer. Cislunar Initial Orbit Determination with Optical Tracklets. In *Advanced Maui Optical and Space Surveillance (AMOS) Technologies Conference*, 2023.

[12] Casey Heidrich and Marcus Holzinger. Universal Angles-Only Cislunar Initial Orbit Determination Using Sparse Grid Collocation. *The Journal of the Astronautical Sciences*, 72(2):16, 2025.

[13] Casey Heidrich and Marcus Holzinger. Initial Orbit Determination for Cislunar Objects with Unknown Maneuvers via Collocation and Nonlinear Programming. *The Journal of the Astronautical Sciences*, 72(4):38, 2025.

[14] Victor Szebehely and Giorgio EO Giacaglia. On The Elliptic Restricted Problem of Three Bodies. *Astronomical Journal, Vol. 69, p. 230 (1964)*, 69:230, 1964.

[15] Allan Kardec de Almeida Junior and Antonio Fernando Bertachini de Almeida Prado. Comparisons between the circular restricted three-body and bi-circular four body problems for transfers between the two smaller primaries. *Scientific Reports*, 12(1):4148, 2022.

[16] Charles Acton, Nathaniel Bachman, Boris Semenov, and Edward Wright. A look towards the future in the handling of space science mission geometry. *Planetary and Space Science*, 150:9–12, 2018.

[17] Jon D Giorgini. Status of the JPL Horizons Ephemeris System. *IAU General Assembly*, 29:2256293, 2015.

[18] Gerard Gómez, Josep J Masdemont, and Josep-Maria Mondelo. Solar system models with a selected set of frequencies. *Astronomy & Astrophysics*, 390(2):733–749, 2002.

[19] Beom Park and Kathleen C Howell. Assessment of dynamical models for transitioning from the Circular Restricted Three-Body Problem to an ephemeris model with applications. *Celestial Mechanics and Dynamical Astronomy*, 136(1):6, 2024.

[20] Anthony Bedford, A Bedford, Wallace L Fowler, and Wallace T Fowler. *Engineering Mechanics: Statics & Dynamics Principles*. Pearson Education, 6th edition, 2024.

[21] John T Betts. *Practical Methods for Optimal Control and Estimation Using Nonlinear Programming*. SIAM, second edition, 2010.

[22] Matthew Kelly. An Introduction to Trajectory Optimization: How to Do Your Own Direct Collocation. *SIAM review*, 59(4):849–904, 2017.

[23] Lorenz T Biegler and Victor M Zavala. Large-scale nonlinear programming using IPOPT: An integrating framework for enterprise-wide dynamic optimization. *Computers & Chemical Engineering*, 33(3):575–582, 2009.

[24] Philip E Gill, Walter Murray, and Michael A Saunders. SNOPT: An SQP algorithm for large-scale constrained optimization. *SIAM review*, 47(1):99–131, 2005.

[25] Transiting Exoplanet Survey Satellite (TESS). `https://exoplanets.nasa.gov/tess/`. Accessed: Aug 2025.

[26] George V Haman III and Anil V Rao. Adaptive Mesh Refinement and Error Estimation Method for Optimal Control Using Direct Collocation. *Journal of Dynamic Systems, Measurement, and Control*, pages 1–36, 2025.

[27] Artemis I Mission Timeline. `https://www.nasa.gov/reference/artemis-i-mission-timeline/`. Accessed: Aug 2025.

[28] Randy A Eckman, Charles Barrett, Amelia L Batcha, and Brian J Killeen. Trajectory Operations Of The Artemis I Mission. In *2023 AAS/AIAA Astrodynamics Specialist Conference*, number AAS 23-363, 2023.

A. APPENDIX: DEFECT CONSTRAINT DERIVATIVES

This appendix outlines analytic derivatives of the Hermite-Simpson constraints with impulsive velocity control. For reference, the constraint equation in Eq. (23) is repeated here:

$$\boldsymbol{g}_k = \boldsymbol{x}_{k+1}^- - \boldsymbol{x}_k^+ - \frac{1}{6}h_k\left(\boldsymbol{f}_k^+ + 4\boldsymbol{f}_{k+1/2} + \boldsymbol{f}_{k+1}^-\right),$$

where the midpoint state is evaluated from Eq. (24) as

$$\boldsymbol{x}_{k+1/2} = \frac{1}{2}(\boldsymbol{x}_k^+ + \boldsymbol{x}_{k+1}^-) + \frac{1}{8}(\boldsymbol{f}_k^+ - \boldsymbol{f}_{k+1}^-).$$

We require derivatives with respect to the pre-control states $\boldsymbol{x}_k^-$ and $\boldsymbol{x}_{k+1}^-$, velocity directions $\boldsymbol{d}_k$, and velocity magnitudes w_k for $k = 1,\ldots,N-1$. First, we note from Eq. (22) that

$$\left(\frac{\partial \boldsymbol{x}_k^+}{\partial \boldsymbol{x}_k^-}\right) = \boldsymbol{I}_n, \quad \left(\frac{\partial \boldsymbol{x}_{k+1}^+}{\partial \boldsymbol{x}_{k+1}^-}\right) = \boldsymbol{I}_n. \tag{38}$$

The state derivatives are defined as

$$\left(\frac{\partial \boldsymbol{g}_k}{\partial \boldsymbol{x}_k^-}\right) = -\left(\frac{\partial \boldsymbol{x}_k^+}{\partial \boldsymbol{x}_k^-}\right) - \frac{1}{6}h_k\left[\left(\frac{\partial \boldsymbol{f}_k^+}{\partial \boldsymbol{x}_k^+}\right)\left(\frac{\partial \boldsymbol{x}_k^+}{\partial \boldsymbol{x}_k^-}\right) + 4\left(\frac{\partial \boldsymbol{f}_{k+1/2}}{\partial \boldsymbol{x}_{k+1/2}}\right)\left(\frac{\partial \boldsymbol{x}_{k+1/2}}{\partial \boldsymbol{x}_k^-}\right)\right], \tag{39a}$$

$$\left(\frac{\partial \boldsymbol{g}_k}{\partial \boldsymbol{x}_{k+1}^-}\right) = \left(\frac{\partial \boldsymbol{x}_{k+1}^+}{\partial \boldsymbol{x}_{k+1}^-}\right) - \frac{1}{6}h_k\left[\left(\frac{\partial \boldsymbol{f}_{k+1}}{\partial \boldsymbol{x}_{k+1}^+}\right)\left(\frac{\partial \boldsymbol{x}_{k+1}^+}{\partial \boldsymbol{x}_{k+1}^-}\right) + 4\left(\frac{\partial \boldsymbol{f}_{k+1/2}}{\partial \boldsymbol{x}_{k+1/2}}\right)\left(\frac{\partial \boldsymbol{x}_{k+1/2}}{\partial \boldsymbol{x}_{k+1}^-}\right)\right]. \tag{39b}$$

At the midpoint state, we have from Eq. (24)

$$\left(\frac{\partial \boldsymbol{x}_{k+1/2}}{\partial \boldsymbol{x}_k^-}\right) = \frac{1}{2}\left(\frac{\partial \boldsymbol{x}_k^+}{\partial \boldsymbol{x}_k^-}\right) + \frac{1}{8}\left(\frac{\partial \boldsymbol{f}_k^+}{\partial \boldsymbol{x}_k^+}\right)\left(\frac{\partial \boldsymbol{x}_k^+}{\partial \boldsymbol{x}_k^-}\right), \tag{40a}$$

$$\left(\frac{\partial \boldsymbol{x}_{k+1/2}}{\partial \boldsymbol{x}_{k+1}^-}\right) = \frac{1}{2}\left(\frac{\partial \boldsymbol{x}_{k+1}^+}{\partial \boldsymbol{x}_{k+1}^-}\right) - \frac{1}{8}\left(\frac{\partial \boldsymbol{f}_{k+1}^+}{\partial \boldsymbol{x}_{k+1}^+}\right)\left(\frac{\partial \boldsymbol{x}_{k+1}^+}{\partial \boldsymbol{x}_{k+1}^-}\right). \tag{40b}$$

Next, for the impulsive control variables, let us define $m = n/2$. We have the following derivatives from Eq. (22)

$$\left(\frac{\partial \boldsymbol{x}_k^+}{\partial \boldsymbol{d}_k}\right) = \begin{bmatrix}\boldsymbol{0}_{m\times m} & w_k\boldsymbol{I}_{m\times m}\end{bmatrix}^{\mathrm{T}}, \quad \left(\frac{\partial \boldsymbol{x}_k^+}{\partial w_k}\right) = \begin{bmatrix}\boldsymbol{0}_m^{\mathrm{T}} & \boldsymbol{d}_k^{\mathrm{T}}\end{bmatrix}^{\mathrm{T}}, \tag{41}$$

where it is noted that the pre-control states $\boldsymbol{x}_{k+1}^-$ do not depend on the velocity control variables. The control derivatives are

$$\left(\frac{\partial \boldsymbol{g}_k}{\partial \boldsymbol{d}_k}\right) = -\left(\frac{\partial \boldsymbol{x}_k^+}{\partial \boldsymbol{d}_k}\right) - \frac{1}{6}h_k\left[\left(\frac{\partial \boldsymbol{f}_k^+}{\partial \boldsymbol{x}_k^+}\right)\left(\frac{\partial \boldsymbol{x}_k^+}{\partial \boldsymbol{d}_k}\right) + 4\left(\frac{\partial \boldsymbol{f}_{k+1/2}}{\partial \boldsymbol{x}_{k+1/2}}\right)\left(\frac{\partial \boldsymbol{x}_{k+1/2}}{\partial \boldsymbol{d}_k}\right)\right], \tag{42a}$$

$$\left(\frac{\partial \boldsymbol{g}_k}{\partial w_k}\right) = -\left(\frac{\partial \boldsymbol{x}_k^+}{\partial w_k}\right) - \frac{1}{6}h_k\left[\left(\frac{\partial \boldsymbol{f}_k^+}{\partial \boldsymbol{x}_k^+}\right)\left(\frac{\partial \boldsymbol{x}_k^+}{\partial w_k}\right) + 4\left(\frac{\partial \boldsymbol{f}_{k+1/2}}{\partial \boldsymbol{x}_{k+1/2}}\right)\left(\frac{\partial \boldsymbol{x}_{k+1/2}}{\partial w_k}\right)\right]. \tag{42b}$$

Now, for the midpoint derivatives with respect to the control direction, we have

$$\left(\frac{\partial \boldsymbol{x}_{k+1/2}}{\partial \boldsymbol{d}_k}\right) = \frac{1}{2}\left(\frac{\partial \boldsymbol{x}_k^+}{\partial \boldsymbol{d}_k}\right) + \frac{1}{8}\left(\frac{\partial \boldsymbol{f}_k^+}{\partial \boldsymbol{x}_k^+}\right)\left(\frac{\partial \boldsymbol{x}_k^+}{\partial \boldsymbol{d}_k}\right), \tag{43a}$$

$$\left(\frac{\partial \boldsymbol{x}_{k+1/2}}{\partial w_k}\right) = \frac{1}{2}\left(\frac{\partial \boldsymbol{x}_k^+}{\partial w_k}\right) + \frac{1}{8}\left(\frac{\partial \boldsymbol{f}_k^+}{\partial \boldsymbol{x}_k^+}\right)\left(\frac{\partial \boldsymbol{x}_k^+}{\partial w_k}\right). \tag{43b}$$

These expressions complete the analytic Jacobian for Eq. (23).

Approved for public release; distribution is unlimited. Public Affairs release approval AFRL-2025-4052.